Materials Horizons

ROYAL SOCIETY OF CHEMISTRY

COMMUNICATION

View Article Online
View Journal | View Issue



Cite this: *Mater. Horiz.*, 2025, **12**, 5733

Received 18th February 2025,
Accepted 28th April 2025

DOI: 10.1039/d5mh00293a

rsc.li/materials-horizons

# Synergistic effects in ambipolar blends of mixed ionic–electronic conductors†

Eyal Stein, [a] Sasha Simotko, [a] Yogesh Yadav, [a] Priscila Cavassin, [b] Iain McCulloch, [cd] Natalie Banerji [b] and Gitti L. Frey *[a]

**Organic mixed ionic–electronic conductors (OMIECs) are extensively utilized in bioelectronics, serving as essential components for converting biological signals into electronic ones. In the realm of ambipolar OMIECs, which support the transport of both electrons and holes, recent studies have introduced a novel blend approach to simplify fabrication and enhance tunability. However, these systems remain scarce, and the urge to advance blend-based OMIEC research is still emerging. Here, we present an extensive investigation of a polymer–fullerene ambipolar system, revealing the remarkable relationship between blend microstructure and system performance. Our results demonstrate that the capacitance and mobility of the blend components exhibit synergistic enhancements, surpassing the values observed in pristine materials. Additionally, the transient response time indicates a significant advantage for blends over pristine materials. These findings are elucidated through a schematic illustration of the blend morphology, providing profound insights into the properties of this system. This comprehensive study paves the way for the improved design of ambipolar OMIECs for use in bio-interfaces, advanced sensing applications, and innovative electronic devices.**

**New concepts**

This work introduces a novel approach to enhancing the performance of organic mixed ionic–electronic conductors (OMIECs) through a blend approach. The key concept demonstrated is that blending can synergistically improve both the ionic and electronic properties of the system, leading to enhanced capacitance, mobility, and ionic diffusion compared to pristine materials in organic electrochemical transistors (OECT). By investigating the structure–property relationships in the blend, we show that local chain aggregation and changes in the crystallinity play crucial roles in these improvements. Additionally, the transient response time of the blend system was significantly better than that of individual components, revealing the potential for tunable ionic diffusion. This research differentiates itself from previous studies by providing a detailed analysis of how blend microstructure influences the performance of ambipolar OECTs, offering a deeper understanding of the interplay between morphology and conductivity. The work provides valuable insights into how the blending strategy can optimize both electronic and ionic transport properties in OMIECs for OECTs, advancing the field of organic materials for electronic and bioelectronic applications.

## 1. Introduction

Organic mixed ionic–electronic conductors (OMIECs) are materials capable of transporting both ions and electrons (or holes), a property that makes them highly suitable for a variety of bioelectronic devices.[1–3] These devices, such as organic electrochemical transistors (OECTs), leverage OMIECs to transduce biological signals into electronic outputs in real-time.[4] The unique physics of OMIECs involves coupling of ionic transport and electronic conduction in the bulk of the organic material, offering efficient and incredibly high signal transduction.[5] Commonly, OMIECs exhibit p-type polarity, favoring hole transport, but recent advances have led to the development of n-type and ambipolar variants, expanding their applicability in complex circuits.[6] The rise of ambipolar OMIECs, which can conduct ions and both holes and electrons, represents a significant advancement in the field. Strategies to achieve ambipolar OMIEC materials include molecular design that incorporates both electron-donating and electron-accepting units,[7] and blending different organic semiconductors to combine their respective advantages.[8,9] The blend approach provides enhanced device performance and versatility, while also offering the possibility of synergistic effects. Synergistic effects in ambipolar organic semiconductor blends

[a] *The Science and Engineering of Organic Electronics Research Group, Department of Materials Science and Engineering, Technion – Israel Institute of Technology, Haifa 3200003, Israel. E-mail: gitti@technion.ac.il*
[b] *FemtoMat Research Group, Department of Chemistry, Biochemistry and Pharmaceutical Sciences, University of Bern, Freiestrasse 3, Bern 3012, Switzerland*
[c] *Department of Chemistry, University of Oxford, Oxford OX1 3TA, UK*
[d] *Andlinger Center for Energy and the Environment and Department of Electrical and Computer Engineering, Princeton University, Princeton, USA*

† Electronic supplementary information (ESI) available. See DOI: https://doi.org/10.1039/d5mh00293a

are highly desirable, as they indicate that the blend not only allows for transport of both electrons and holes but also performs better than the sum of its individual components and can offer properties not attainable in the individual materials. For instance, in organic field-effect transistors, ambipolar blends have shown not only balanced hole and electron transport, but also enhanced charge carrier mobilities.[10,11]

Despite the abundance of blends in organic electronic devices, most commonly in organic solar cells (OSCs), the blending approach for ambipolar OMIEC devices is still in its infancy. Various types of blends have been explored in this field, including semiconducting polymers with polymer electrolytes or polyelectrolytes,[12–14] blends of two semiconductors,[8,9] semiconducting polymers with molecular dopants,[15,16] and semiconducting molecules with polymer electrolytes.[17] However, not only are unipolar blends scarce in OMIECs, but ambipolar blends are even rarer due to their higher complexity and studies demonstrating synergistic effects in ambipolar OMIECs are particularly limited. Studies on ambipolar OMIEC blends have not observed significant synergistic effects indicating that the reported blends have not shown an increase in any of the materials' merits compared to the pristine materials.[8,9] The challenge in achieving synergistic effects in ambipolar OMIECs lies in the complex interplay between electronic and ionic transport mechanisms, as well as the morphological considerations that arise from blending different materials.[6,18] Factors such as the molecular weight and size distribution of the polymers,[19] the degree of crystallinity and aggregation,[20] and the nature of the side chains[21] all play crucial roles in determining the overall performance of the blend. Understanding and optimizing these factors is essential for developing high-performance ambipolar OMIECs with synergistic effects.

In this work, we investigate a blend of n-type fullerene and p-type polymer OMIECs to elucidate the relationship between blend composition, microstructure, and performance towards ambipolar performance and synergistic effects. Using time-resolved VIS-NIR absorbance measurements and grazing incidence wide-angle X-ray scattering (GIWAXS), we characterize the doping mechanisms, crystallinity, and orientation of the materials. Our research reveals that the blend components exhibit synergistic enhancements in both capacitance and mobility, outperforming their pristine counterparts. Additionally, the blend system shows faster optical transient response time compared to pristine materials, beneficial for dynamic applications and bioelectronic devices requiring rapid signal processing. The blend microstructure demonstrates a complex interplay between crystalline and amorphous phases, crucial for performance enhancements and efficient charge and ion transport. The enhanced performance of the polymer–fullerene blend underscores its potential for advanced bio-interface materials, sensors, and innovative electronic devices. Our findings pave the way for improved design and application of ambipolar OMIECs, highlighting the importance of continued exploration of blend-based systems for future technological advancements.

# 2. Results and discussion

In this study, we investigate the synergistic effects in ambipolar blends of mixed ionic–electronic conductors, focusing on a polymer–fullerene system comprised of p(g2T-TT) and $PrC_{60}MA$ (Fig. 1(a) and (b)). These materials were chosen for their complementary p and n-type electronic properties respectively, and potential for enhanced performance when combined. Our comprehensive analysis begins with an examination of the transient response time, a critical parameter for understanding the dynamics of charge transport in these blends. We then explore the electronic mobility of both n-type and p-type carriers, which provides insights into the charge transport mechanisms and the impact of blend composition on device performance. The volumetric capacitance is subsequently investigated to elucidate the charge storage capabilities of the blends, a key factor in determining the overall effectiveness of these materials in bioelectronic applications. Throughout our analysis, we employ a range of characterization techniques, including spectroelectrochemistry (SEC), electrochemical impedance spectroscopy (EIS), and X-ray diffraction (XRD), to probe the structural and electronic properties of the blends. By correlating these measurements with device performance, we aim to establish a comprehensive understanding of the structure–property relationships in this ambipolar system.

## 2.1. Transient response time, $\tau$

To fully understand the complex interplay between electronic and ionic transport in ambipolar OMIECs, it is crucial to investigate the dynamics of charge carrier generation and transport under applied electric fields. These processes occur on timescales ranging from milliseconds to seconds, making time-resolved spectroscopic and electrical techniques invaluable for their characterization. With these considerations in mind, we employed two different time-dependent methods and compared their results. The first is time-resolved Vis-NIR absorbance to investigate the electrochemical doping mechanisms in our pristine and blend films, while applying different potentials to the system. The second is transient current response of OECTs upon repeated on–off cycles to investigate the combined electronic and ionic transport mechanisms.

First, the steady-state absorbance in a Vis-NIR spectroelectrochemistry setup (Fig. 1(c)) was recorded for each potential step, as depicted in Fig. S1 and S2 (ESI†). The doping characteristics of the n-type show a positive signature around 560 nm and a negative one around 460 nm, features that are associated with fullerene electroabsorption, *i.e.*, fullerene clusters responding to an electric field.[22] The band rise at $\sim$1000 nm indicates the formation of a fullerene radical anion $C_{60}^{-}$.[23] Both the radical anion formation and the fullerene electroabsorption phenomena observed in the spectra confirm the electrochemical doping of $PrC_{60}MA$.

In a similar manner to our previous study,[9] we compared the measured steady-state spectroelectrochemical results of the blends to a calculated rule-of-mixtures (ROM) spectra (Fig. S3, ESI†) from the pristine materials and their respective weight

 

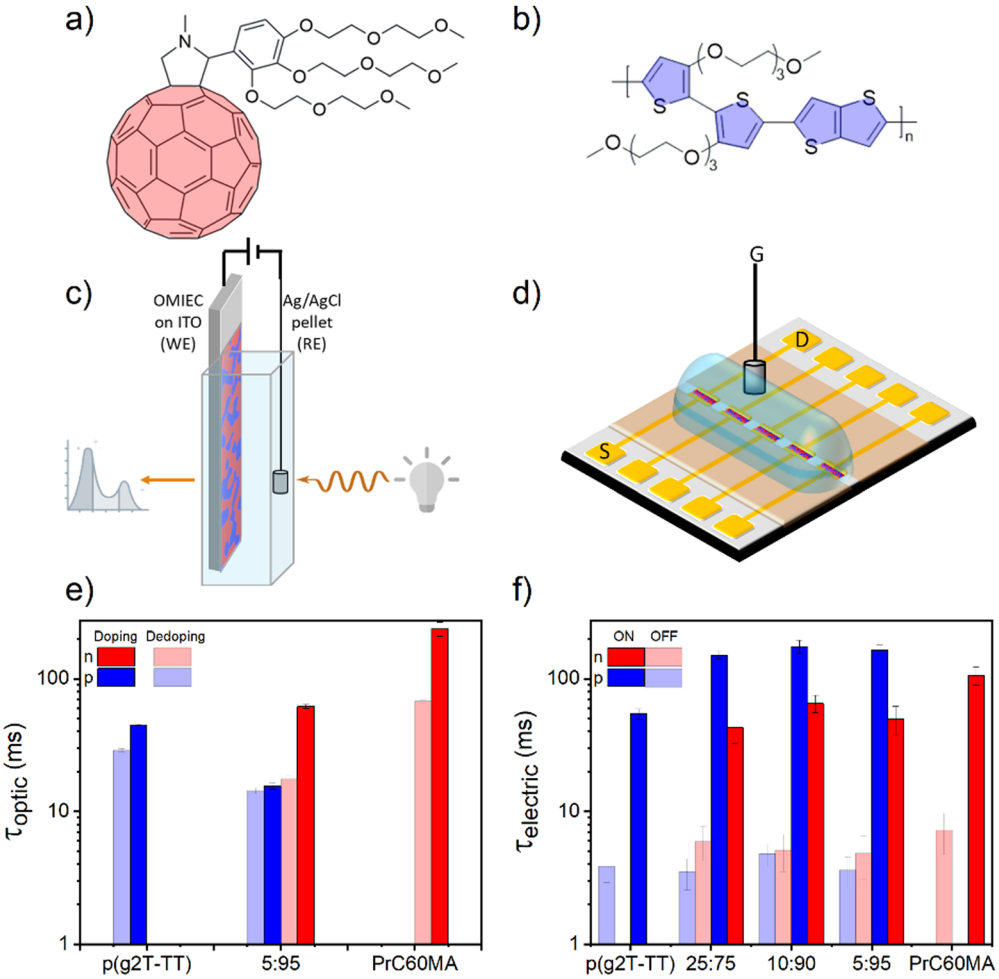


Fig. 1 Transient current response time of OECTs and optical response time. (a) and (b) Molecules used in this work, $PrC_{60}MA$ and p(g2T-TT), respectively. (c) and (d) Schemes of the setups used for the measurements, spectroelectrochemistry and OECTs, respectively. (e) Optical transient response time as measured from changes in the absorbance spectra at different voltage steps. (f) Electrical transient response time as measured from ON–OFF pulsing of the OECTs (Fig. S7, ESI†). Thickness of the films was uniform at 60 nm for all measurements.

fraction (eqn (1) of the experimental section). We noticed that the signature of fullerene electroabsorption is more prominent in the measured spectra, corroborating that this enhanced effect is indeed a result of blending with p(g2T-TT). Regarding the p-type, doping shows a clear band rise centered at ~950 nm which is associated with the formation of a positive polaron, and the subsequent decay of the neutral π–π* transition around 600 nm. In the blends, the same features related to either n- or p-type doping can be observed for negative or positive potentials, respectively, corroborating that both the n-type molecule and the p-type polymer are electrochemically active also in the blends.

Though the ROM calculated spectra had an excellent similarity to the measured spectra, in order to advance to quantitative time-resolved measurements, we sought to reconstruct the exact steady-state absorbance spectra of the 5 : 95 (p-type : n-type) from the distinct spectral signatures of the pristine components. For that we used an analysis method known as Multivariate Curve Resolution by Alternating Least Squares (MCR-ALS) and fitted the spectra to the signatures associated with the n- and p-type features observed in the pristine films (Fig. S4, ESI†). The decomposition demonstrates clearly that the n-type small molecule and the p-type polymer doping are completely independent, with each domain of the film being doped at the same potential and without major changes in their absorbance spectra compared to their pristine films.

We then used the MCR analysis to gain insights into the effect of blending on the doping/dedoping kinetics by investigating the time-resolved concentration changes of the neutral and charged species. We obtained optical time constants of doping (Fig. S5 and Table S1, ESI†) and dedoping (Fig. S6 and Table S2, ESI†) for different films thicknesses of the pristine materials and the 5 : 95 (p-type : n-type) blend, using either mono- or biexponential fitting of the time-resolved concentration changes of the positive charges (voltage step from −0.4 V to +0.3 V) or for the negative charges (voltage step from −0.4 V to −0.9 V).

Examining the optical doping time constants reveals that there is a clear dependency on the film thickness in the measured 20–200 nm range – thicker films are doped slower, confirming that in this range our system operates in an ion-diffusion regime. Moreover, the obtained time constants suggest that the film thickness does not play a significant role in determining the fitting function of the material's optical response. For example, the fitting function for the p-type optical doping and dedoping, in its pristine form and in the blend, is mostly monoexponential. In contrast, doping in pristine $PrC_{60}MA$ fits a biexponential function, whereas in the 5 : 95 blend it features only a single time constant, namely, a monoexponential function. This transition from biexponential to monoexponential response is thought to originate from the expected change in the microstructure, *i.e.*, n-type pristine film has a more heterogeneous microstructure that becomes increasingly homogeneous in the 5 : 95 blend.

Fig. 1(e) compares the average time constants of the mid-range (60 nm thick) pristine and 5 : 95 blend films. Interestingly, we observe that both doping and dedoping become faster in this particular blend, compared to those in the pristine films. Fig. 2 compares the time constants of doping/dedoping in this blend and pristine materials for the various thicknesses measured, where there is also a clear trend that the n- and p-type are doped and dedoped faster for all the thicknesses. Since optical doping and dedoping are closely related to the ion kinetics in and out of the film, these findings confirm that blending here enables faster ion transport.

The optical measurements encompass two main processes that generally exist in OMIECs, that is, ion transport and ionic–electronic coupling. However, for bioelectronic devices, we require further understanding of the third fundamental process – electronic transport. The spectroelectrochemical experiments cannot directly capture this process because of the dimensionality of the setup (with only two electrodes). Therefore, we turn to the fabrication and measurement of organic electrochemical transistors (OECTs).

We fabricated OECTs based on pristine materials and various blends and performed on–off switching cycles (Fig. S7, ESI†) to examine the turn-on ($\tau_{on}$) and turn-off ($\tau_{off}$) time constants of the drain current $I_d$ (Fig. 1(d) and (f)). These were extracted from the data using biexponential fitting for the ON step and monoexponential fitting for the OFF step (see experimental). The two-stage ON step represents vertical doping

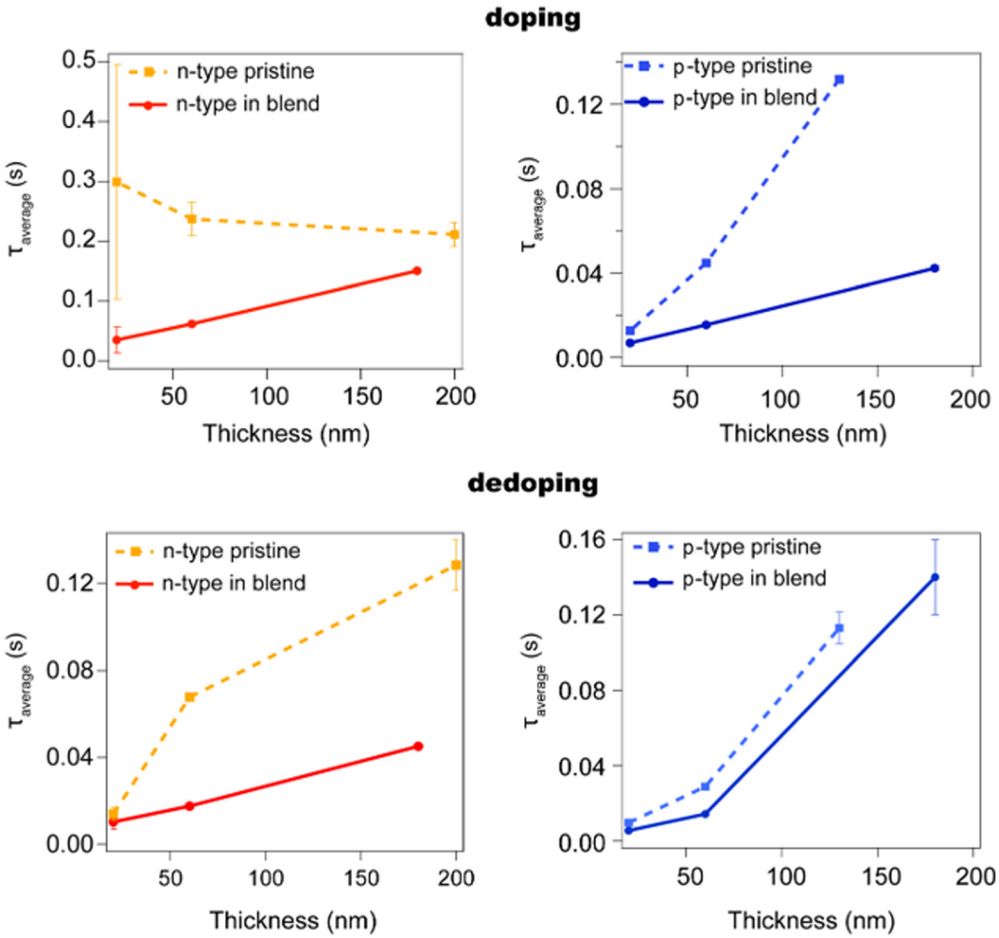


Fig. 2 Optical doping and dedoping average time constants of the pristine and blend films, related to the kinetic traces shown in Fig. S5 and S6 (ESI†) and the time constants in Table S2 (ESI†).

 

followed by molecular structural relaxation or charge reorganization, whereas the one-stage OFF step represents vertical doping alone.[24] To properly compare time constants between different devices, we kept the driving force for the ON and OFF cycles constant across all compositions, in a similar manner to a study by Guo *et al.*[24] Namely, the potential difference between the threshold voltage and the ON and OFF voltages, $|V_{th} - V_{ON}|$ and $|V_{th} - V_{OFF}|$, were kept constant (Table S3, ESI†).

The electrical time constants show opposite trends for the n-type and p-type polarities, whereas in the optical time constants the trends are similar. While the n-type $\tau_{on}$ is two times faster in the blends than the pristine $PrC_{60}MA$, the p-type $\tau_{on}$ is three times slower than that of pristine p(g2T-TT). Since our blends are clearly acceptor dominant, the significant improvements of the n-type $\tau_{on}$ are surprising because the acceptor content does not change largely. We hypothesize that the origin of this faster response in the blends is due to improved ion-diffusion pathway formed by the bulk-heterojunction-like structure.[25]

On the p-type side, the slower $\tau_{on}$ in the blends demonstrates that under our measurement conditions, the rate determining step in the OECT p-type response is the hole transport and not the ion transport, as also shown and explained in a recent work by Keene *et al.*[26] In that study, the researchers found that in poorly ordered polymers at low doping potentials, holes reside in isolated crystalline domains and therefore hopping between trap states and crystalline domains becomes challenging. Under standard OECT potentials, low hole concentration may be a result of the reduced electric field operating in long device channels. Going back to our results, the fact that the blends are mostly n-type and only contain 5–25% of p-type polymer chains could lead to similar conditions as in the mentioned study, since the polymer chains are scarcer and more isolated and the doping potential is low (0.3 V). Therefore, it is no surprise that the hole transport, and not ion-transport, is the device turn-on limiting factor and the p-type operation is slowed down in the blends.

The turn-off time constant $\tau_{off}$ does not display any clear trend throughout compositions, though it is much faster. This is despite the fact that driving force for turn-off is weaker than for turn-on since $|V_{th} - V_{OFF}| < |V_{th} - V_{ON}|$ (0.1 V *vs.* 0.25 V respectively). Our results agree with the latest findings showing experimentally that it is enough for the conductive channel to be broken by a thin dedoped slice near the electrode to turn off the device.[24] This cited research also strengthens its conclusions by concurrently monitoring the optical and electrical responses of OECTs, revealing that dedoping occurs faster near the source electrode. Though already turned-off, the OECT optical measurement showed that dedoping continues, supporting the claim that when a thin slice of conducting channel is severed, the entire OECT is turned-off but dedoping continues. Accordingly, our results show that the electrical $\tau_{on}$ and optical doping, except for the p-type response in the blends, are of the same order of magnitude, hence the rate limiting process is the ionic diffusion inside the channel.

The results in this section highlight that blending n- and p-type mixed conductors can result in improved ion kinetics in the overall system, leading to faster optical and electrical transient response which are key parameters in the ambipolar OMIECs. To produce faster switching devices and address not only ion kinetics, but also electronic transport, we must turn to the figure that encompasses both requirements – mobility.

### 2.2. Electronic mobility, $\mu$

In ambipolar blends in OFETs, the general trends for n- and p-type mobility as a function of the blend ratio are usually straightforward and decrease monotonously as the weight percent of the corresponding component decreases.[8,10,11,27–29] Namely, though the blend microstructure could be complex, it does not typically have a significant effect on the mobility of each component. Now we turn to study the effect of composition on the mobility in the ambipolar OECT blends. As mobility cannot be extracted from OECT measurements alone, but rather the product $\mu C^*$, we used a standard procedure[19,30,31] where electrochemical impedance spectroscopy (EIS) is performed to extract $C^*$ followed by the calculation $\mu = \frac{\mu C^*}{C^*}$.

Depicted in Fig. 3, the n- and p-type mobilities in the ambipolar blends exhibit very different behaviors. The n-type mobility of the pristine $PrC_{60}MA$ is high, $\sim$0.36 [$cm^2\ V^{-1}\ s^{-1}$], and drops to about half its original value upon the addition of only 5% wt p(g2T-TT). It then remains rather constant when added even more polymer up to 25% wt. In contrast to $PrC_{60}MA$, the p-type mobility of p(g2T-TT) begins at $\sim$1.8 [$cm^2\ V^{-1}\ s^{-1}$] for the pristine material, yet upon blending with a significant amount of fullerene, 75% wt, the mobility surges to 2-times its original value. Following the addition of even more $PrC_{60}MA$ the p-type mobility decreases, yet even at only 5% wt the p-type is still higher than pristine p(g2T-TT).

To fully understand the origins of the mobility trends in both p- and n-type polarities, we turn to structural and spectral techniques. X-ray based techniques can shed light on the microstructure-mobility relation for $PrC_{60}MA$'s crystallites, whereas we suggest that the p-type mobility is related to aggregation of the polymer chains and their low content in the blends.

**2.2.1. n-Type mobility.** Since the blends are composed of a majority n-type phase, we propose that the microstructure of $PrC_{60}MA$ must play a key role in determining the n-type mobility behavior. Therefore we turn to X-ray-based techniques to probe the system's crystalline structure. Grazing incidence wide-angle X-ray scattering (GIWAXS) was first employed to gain insights on the general crystalline structures of both pristine materials and their blends.

In line with previous studies, pristine p(g2T-TT) crystallites possess predominantly edge-on orientation and pristine $PrC_{60}MA$ crystallites adopt a preferred orientation where the *c*-axis is predominantly perpendicular to the substrate (Fig. 4(a)). Out-of-plane and in-plane linecuts were extracted from the GIWAXS data to calculate *d*-space and assign *hkl* miller indices, as depicted in Fig. 4(b) and (c). The miller indices for $PrC_{60}MA$ were assigned assuming a general

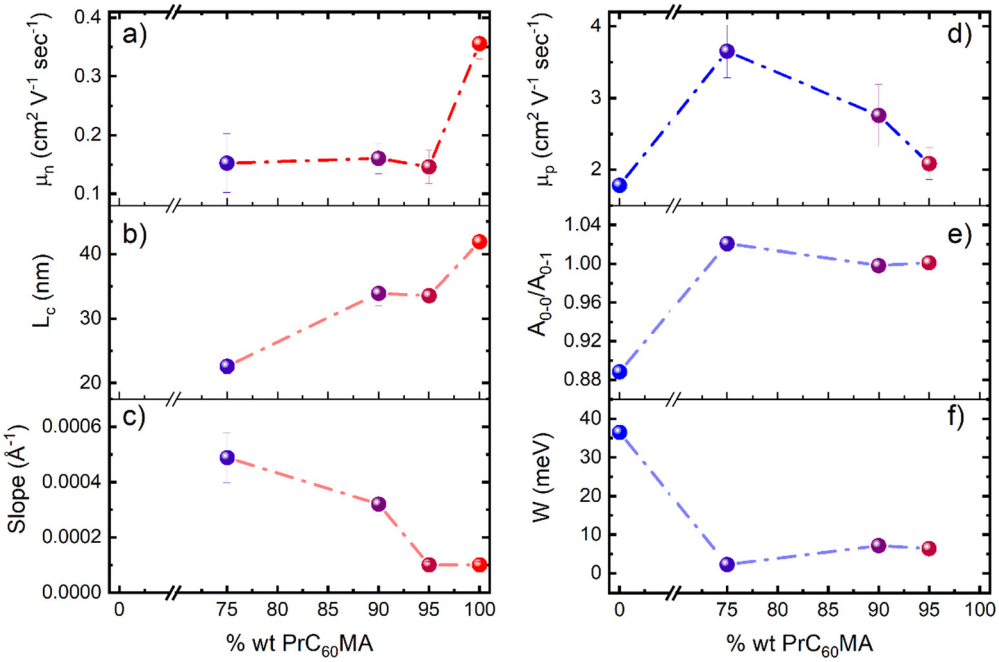


Fig. 3 Mobility-structure relationships in the $PrC_{60}MA$:p(g2T-TT) blend systems. (a) and (d) Electronic mobility of the n- and p-type charges as a function of the blend composition, respectively. (b) The coherence length of $PrC_{60}MA$ crystallites in the (00*l*) reflections and (c) the slope of the cumulative disorder term change over different peak orders (Fig. S9, ESI†). (e) The ratio between the 0–0 and 0–1 vibronic Gaussian peak intensities and (f) the excitonic interchain bandwidth as fitted from the vibronic model developed by Spano *et al.*[32]

tetragonal crystal lattice system as previously reported for similar glycolated fullerenes[33,34] (Fig. S11 and S12, ESI†).

The X-ray measurements reveal pristine $PrC_{60}MA$ lattice parameters of: $a = b = 10.1$ Å, $c = 24.5$ Å (Table 2), demonstrating a slightly contracted *c*-axis compared to a nearly identical glycolated fullerene, PTEG-2 ($c = 27$ Å).[33] Under the assumption of a tetragonal lattice system, where the *c*-axis dimension is determined by the length of the side-chains, this finding is coherent with the mildly shorter side-chains of $PrC_{60}MA$ compared with PTEG-2. Unfortunately, the (100) peak for p(g2T-TT) could not be resolved in the blends due to its low intensity and overlap with the $PrC_{60}MA$ (002) peak. It is clear from Table 2 that blending in these compositions does not affect $PrC_{60}MA$ crystallite's internal structure, as *d*-spaces do not change significantly upon blending even down to 75% $PrC_{60}MA$.

Two other phenomena are visible in the data; one is the gradual loss of $PrC_{60}MA$'s crystallites preferred orientation; the other is the general decrease in its degree of crystallinity. The former is seen in Fig. 4(a) as a gradual shift from dot-like GIWAXS to smeared dots and rings when moving from $PrC_{60}MA$ to p(g2T-TT); while the latter shows as a qualitative decrease in peak intensity in Fig. 4(a)–(c), for example $PrC_{60}MA$'s (110), (200) and (310) peaks. The preferred orientation of $PrC_{60}MA$'s crystallites causes their (00*l*) normal to coincide with that of the substrate. This orientation plays a significant role in the mobility of electrons through the fullerene phase, since according to the approximated crystalline structure (Fig. S12, ESI†) the (00*l*) planes have the highest fullerene conjugated system density and hence best support electronic transport parallel to the substrate plane and along the OECT channel. Hence, once orientation is gradually lost, as seen when adding increasing amounts of p(g2T-TT) to the blends, n-type electronic mobility swiftly decreases.

Another technique used to understand the drop in n-type mobility was 1-dimensional X-ray diffraction (1D-XRD). Using 1D-XRD to analyze integral peak breadth for decoupling coherence length from disorder-related terms (Fig. S9, ESI†), similarly to previous studies,[9] we noticed that the (00*l*) coherence length decreases and the cumulative-disorder-related slope increases as $PrC_{60}MA$'s content is reduced (Fig. 3(b) and (c)). Though it is not a perfect measure for organic crystallite size, the crystalline coherence length has a direct impact on the electronic charge carrier mobility – reduced coherence length leads to reduced mobility since charge carriers scatter over shorter length scales. The reduction in coherence length could explain the n-type mobility drop upon blending with the polymer. However, Fig. 3(a) shows that the combined inter-crystalline and intra-crystalline charge mobility is constant throughout all blends where crystallites are in the range of 20–30 nm, indicating that these effects balance each other out when it comes to mobility. Interestingly, the opposite trends for coherence length and linear slope suggest that cumulative disorder is more significant in smaller $PrC_{60}MA$ crystallites. This finding is in line with the common models for crystallinity,[35] as smaller grains introduce more grain boundaries which are inherent structural defects.

Overall, the key finding in this section is that upon blending with an increasing amount of polymer, the $PrC_{60}MA$ crystallites

 

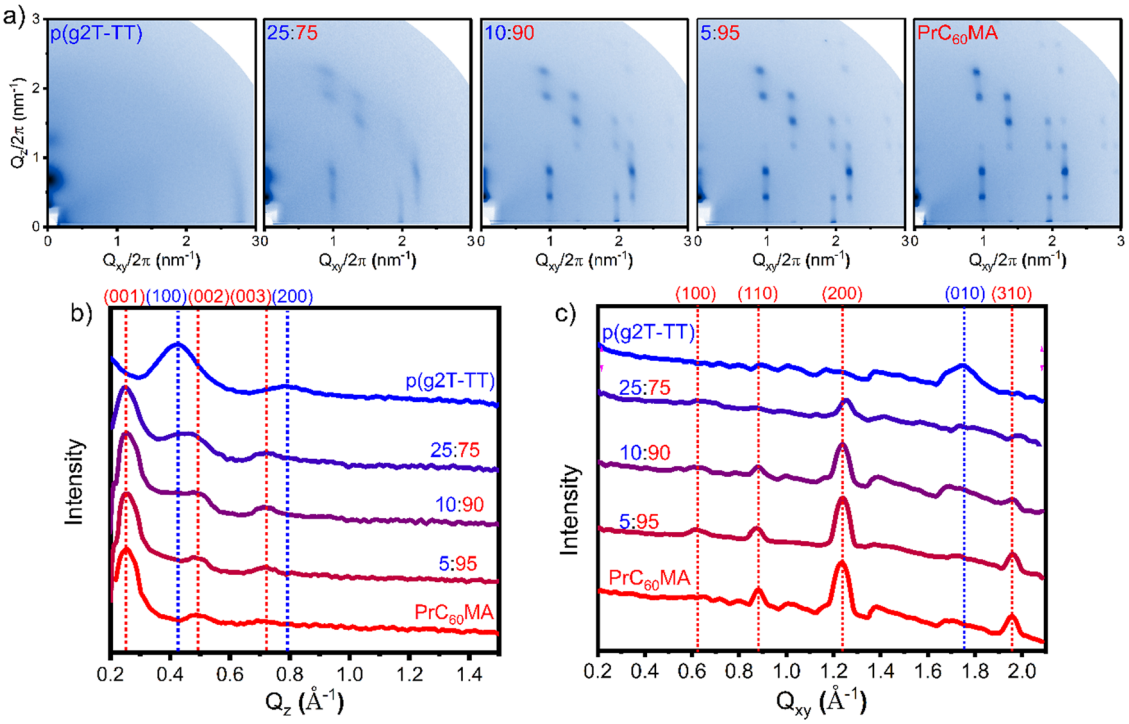


Fig. 4 Microstructural characterization of the system with (a) GIWAXS patterns and the corresponding (b) out-of-plane and (c) in-plane linecuts.

gradually lose preferred orientation and are partially replaced with an amorphous phase, though the remaining crystallites are unchanged in their internal structure. Namely, adding the p(g2T-TT) polymer to $PrC_{60}MA$ neat film increases the homogeneity and isotropy of the layer, as was also postulated in the previous section where the optical doping process of $PrC_{60}MA$ became monoexponential upon blending, rather than biexponential in the pristine.

**2.2.2. p-Type mobility.** To understand the trend observed in the p-type mobility (Fig. 3(d)), namely, the rise in mobility for 25% wt p-type followed by a decay down to 5% wt p-type, we turn to our spectroelectrochemical results. The measured differential absorbance spectra on Fig. S3 (ESI†) show that the reduction in the π–π* neutral species has a similar shape to the calculated spectra (ROM of pristine materials), yet there is a slight change in the 600 and 650 nm peak ratio. Using an H-aggregate vibronic absorption model developed by Spano *et al.*,[32] we fit the data to a series of Gaussian functions that represent vibronic (0–0, 0–1, 0–2 *etc.*) and polaronic transitions in the polymer (Fig. S13, ESI†). To determine the type of aggregation of the polymer chains, either J- or H-type, the Gaussians to be considered are 0–0 and 0–1, with the ratio between them, $A_{00}/A_{01}$, indicating the aggregate type (Fig. 3(e), (f) and Table 1). When $A_{00}/A_{01} < 1$ the polymer chains adopt a more H-type aggregation, with higher interchain interactions. In contrast, $A_{00}/A_{01} > 1$ indicates a more J-type aggregation, with higher intrachain through-bond interactions.

According to this ratio, the pristine p-type polymer adopts a dominant H-aggregated morphology with a ratio of 0.888 (Fig. 3(e)). Using that polymer in blends, where its content is 25% and lower, that ratio changes to ~1 and therefore suggests that the polymer chains adopt a higher J-type aggregates than their pristine p(g2T-TT) counterpart. Isolated polymer chains act as 1D semiconductors and their presence in the film may also contribute to the more J-like character in the blends. Though we could not measure the change in the crystalline character of p(g2T-TT) in the blends, another work showed a direct relation between lower crystallinity and higher

Table 1 Fitting results for ΔAbs of p(g2T-TT) doping at +0.3 V using $\lambda^2$ = 0.97

| % wt p(g2T-TT) | $A_{00}/A_{01}$ | $W$ [meV] |
|---|---|---|
| 100 | 0.888 | 36.5 |
| 25 | 1.021 | 2.3 |
| 10 | 0.998 | 7.2 |
| 5 | 1.001 | 6.4 |

Table 2 Peak centers fit from GIWAXS and calculated *d*-spaces

| Index | | p(g2T-TT) | 25 : 75 | 10 : 90 | 5 : 95 | $PrC_{60}MA$ |
|---|---|---|---|---|---|---|
| (100)[a] | $q$(Å$^{-1}$) | 0.423 | 0.614 | 0.615 | 0.634 | 0.621 |
| | $d$(Å) | 14.8 | 10.2 | 10.2 | 9.9 | 10.1 |
| (010)[b] | $q$(Å$^{-1}$) | 1.749 | | | | |
| | $d$(Å) | 3.59 | | | | |
| (001) | $q$(Å$^{-1}$) | | 0.251 | 0.257 | 0.251 | 0.257 |
| | $d$(Å) | | 25.1 | 24.5 | 25.1 | 24.5 |

[a] The (100) peak is extracted from out-of-plane for p(g2T-TT) and in-plane for $PrC_{60}MA$. [b] The (100) and (010) planes are equivalent in $PrC_{60}MA$'s tetragonal structure.

J-aggregation in a D–A polymer,[36] further supporting the possibility of isolated polymer chains in our films.

From the fitting of differential absorbance spectra we also extracted the exciton bandwidth $W$ (Fig. 3(f)). The exciton bandwidth is a measure of the spread of excitonic energy within the H-aggregate, indicating how the energy levels of the excitons are distributed due to the interactions between the chains in the aggregate. The exciton interchain bandwidth $W$ serves as a sensitive indicator of polymer conjugation length, as it inversely correlates with it, indicating that excitons with greater delocalization along a conjugated chain exhibit reduced interchain bandwidth.[37]

The $W$ analysis in Fig. 3(f) shows that the exciton interchain bandwidth decreases by an order of magnitude from 36.5 meV in the pristine p(g2T-TT) to 2–6 meV in the blends, correlated with the increase in J-aggregate character of the polymer chains that we found earlier. When p(g2T-TT) exhibits both a lower exciton interchain bandwidth and higher J-like aggregation, as was also found in a study with similar molecules,[18,20,38] it means that the polymer chains are becoming more planar in a way that promotes a more efficient charge transport. The combination of weaker π–π interactions (indicated by the lower exciton bandwidth) and the favorable head-to-tail alignment of molecules (J-type aggregation) creates an optimal environment for hole mobility. This synergistic effect enhances the overall mobility of the material by facilitating the movement of holes through the polymer matrix more effectively even at low polymer concentrations.

The general increase in p-type mobility when moving from pristine p(g2T-TT) to its blends is well explained. However, after peaking at 75 : 25 the p-type mobility decreases for the 90 : 10 and 95 : 5 blends, which has to be accounted for. Since all of the studied blends show similar vibronic peak ratio and exciton bandwidth, these cannot explain the drop in mobility and we associate the observed decrease in polythiophene mobility in blends with higher fullerene content than 75% wt with impaired chain connectivity of the polymer chains. At lower p-type concentrations, the polymer chains are less interconnected, which hinders effective charge transport. This reduction in chain connectivity is likely due to the disruption of the polymer network by the high concentration of fullerene molecules and crystallites, which can lead to phase separation and reduced polymer crystallinity. Studies have shown that the nanoscale arrangement and intercalation of fullerene molecules within the polymer matrix significantly affect the charge transport properties. Specifically, at higher fullerene loadings, the formation of a pure electron-transporting phase is favored, which can disrupt the continuous pathways necessary for efficient hole transport in the polymer phase.[39–41] Overall, we suggest that the polymer chains do not change their packing significantly as their content in the blend is reduced, yet they are more ordered and planar which keeps the mobility high even at low concentrations.

Interestingly, the trends in mobility are exactly opposite to the trends in OECT transient response time. While the n-type mobility decreases in blends, the electrical transient n-type response is faster, and though the p-type mobility increases in blends the electrical transient p-type response is slower. The discrepancy between electronic mobility and electrical time constant could be resolved if we note the ionic species in the process – in the n-type case the ionic injection and diffusion/drift may improve while in the p-type case they may decrease, meaning the electronic mobility is less significant in determining the transient OECT behavior. To sum up, these phenomena suggest ionic transport, rather than electronic transport, is dominating the device behavior.

The exploration of charge carrier mobility in our ambipolar mixed conductor blend provides crucial insights into the material's electronic properties. While mobility offers a measure of how quickly charges can move through the material, it is equally important to consider the blend's ability to store these charges. This storage capacity, quantified by volumetric capacitance ($C^*$), plays a vital role in determining the overall performance of the mixed conductor in electronic devices. The interplay between mobility and capacitance is particularly significant in organic electrochemical transistors (OECTs), where both parameters contribute to the device's transconductance. As we transition our focus to capacitance, we will examine how this property complements mobility in shaping the synergistic effects observed in our ambipolar blend.

### 2.3. Volumetric capacitance, $C^*$

As a representative of the ion–electron coupling throughout the volume of the channel, the changes in volumetric capacitance are complementary to the mobility data and should offer a wider understanding of the electrochemical properties of our system. To find the volumetric capacitance we used electrochemical impedance spectroscopy (EIS, see experimental section) and averaged the results over 2 measuring pads for each composition (Fig. S15 and S19, ESI†). We performed the measurement analysis and capacitance calculation using two different methods – equivalent circuit fitting and using raw series capacitance – and compared their results. In the equivalent circuit fitting method, we modeled the p-type behavior using the common Randles circuit $R_s(R_pC_p)$, where $R_s$ is the solution resistance, $R_p$ the polymer resistance and $C_p$ the polymer capacitance (Fig. S14b, ESI†). The n-type results showed a more complex behavior fitting for a two RC time constants circuit, so we modeled it using a second-order Voigt circuit $R_s(R_pC_p)(RQ)$, where $R_s$, $R_p$ and $C_p$ are the same as in the Randles circuit (Fig. S14a, ESI†). The additional presence of a second resistor, $R$, and constant phase element (CPE), $Q$, which is a non-ideal capacitor, suggests that charging and ion injection take place at the interface between the polymer and electrolyte, resulting in an inhomogeneous double-layer capacitance.[14,42] It is noteworthy that since the CPE exponent was $<0.65$ in all n-type measurements, which is far enough from an ideal capacitor (where $n = 1$), its contribution to the overall capacitance was negligible.[10,41]

The fitting results for every composition discussed here are given in Table S4 (ESI†). In addition to equivalent circuit fitting, we also used the raw series capacitance ($C_s$) that is calculated

 

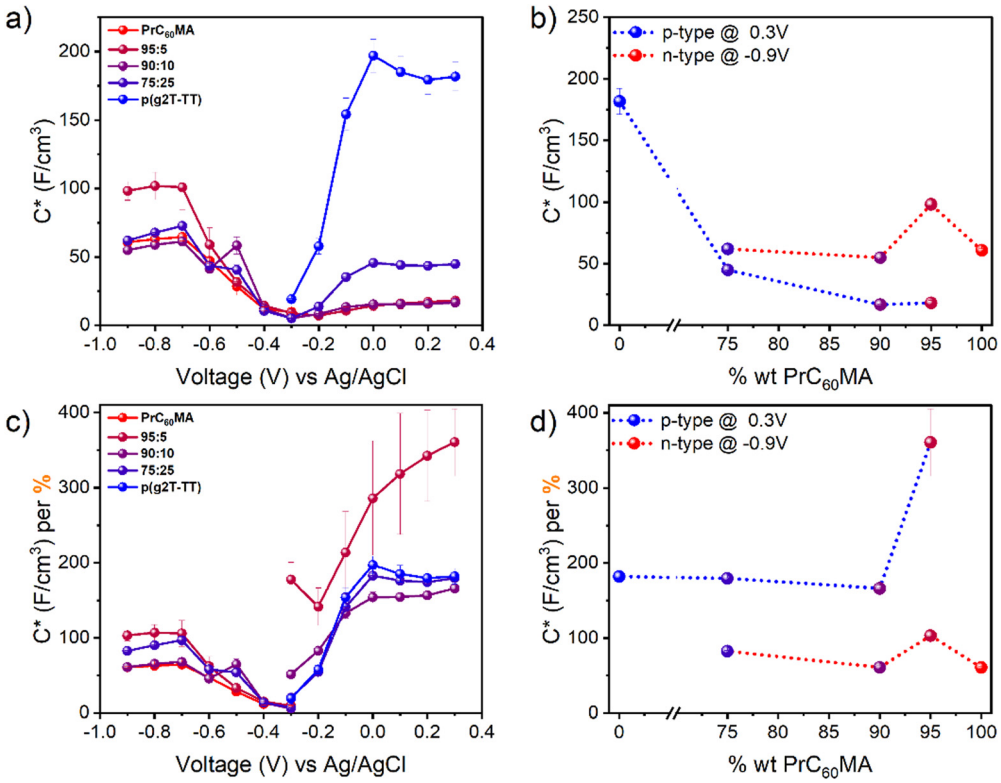


Fig. 5 Volumetric capacitance results from Electrochemical Impedance Spectroscopy measurements. (a) and (c) Volumetric capacitance over applied voltage and normalized to material % wt, respectively. (b) and (d) Volumetric capacitance at maximum doping voltage (0.3 V and −0.9 V for p- and n-type, respectively) over compositions and normalized to material % wt, respectively.

automatically in the measuring software (PSTrace, Palmsens BV) on the basis of the imaginary component of impedance according to eqn (6) of the experimental section. These results were found to be very similar to those from the equivalent circuit fitting at high doping potentials, corroborating that our models were assigned correctly. Though both methods, equivalent circuit and raw series capacitance, produced similar capacitance values, we decided for further calculations to use only the series capacitance as this value is extracted using less mathematical maneuvers and physical assumptions on the system.

Fig. 5(a) shows that, as expected, in all compositions the volumetric capacitance increases from the film's undoped state at −0.3 V *vs.* Ag/AgCl in both directions of the applied potential – either p-doping or n-doping. However, this increase in volumetric capacitance reaches a peak, followed by a slight decrease at higher potentials, which can be attributed to several factors related to high doping levels. High doping levels can introduce energetic and structural disorder, which can negatively impact the material's ability to store charge. Moreover, at high charge densities, electron–cation and hole–anion interactions at the electrolyte/semiconductor interface can alter the potential energy landscape, leading to decreased capacitance.[1] Finally, high doping levels can introduce defects or trap states, capturing charge carriers and reducing the effective capacitance.

Interestingly, the rise in capacitance with an increasingly higher doping potential, for both p- and n-type, begins immediately when moving away from the neutral potential of −0.3 V, while the turn-on of the OECTs (Fig. S8, ESI†) starts at higher doping potentials. This means that capacitance increases at lower doping potentials, and mobility increases only at higher doping potentials, lagging behind capacitance. This offset suggests that there is a significant concentration of low mobility electronic charge carriers at their corresponding transport levels, and that these low mobility states need to be filled before high mobility electronic charge carrier states can be occupied.[26]

Taking the maximum doping potential, *i.e.* 0.3 V and −0.9 V for p- and n-type, respectively, we can plot the change in maximal capacitance over compositions as in Fig. 5(b). While another ambipolar blend OMIEC system in recent research shows a linear change in volumetric capacitance over compositions,[8] in our study this is not the case. The p-type volumetric capacitance decreases from 182 [F cm$^{-3}$] for pristine p(g2T-TT) down to 45 [F cm$^{-3}$] and 17 [F cm$^{-3}$] for 25% and 10% p(g2T-TT), respectively. Fig. 5(d) shows the volumetric capacitance normalized to wt %, demonstrating that the effective capacitance in p-type operation remains similar down to 10% p(g2T-TT), which reflects a similar number of actively-doped monomer units contributing to the overall p-type capacitance. Remarkably, the p-type volumetric capacitance in the 5 : 95 blend reflects a 2-fold increase in the relative number of doped monomer units compared to the other compositions. We suspect this is because at high dilution levels, the p–n

phase separation might have created unique interfacial regions where ion accessibility and electronic conductivity are enhanced beyond what would be expected from simple linear scaling.

The n-type volumetric capacitance is 61 [F $cm^{-3}$] for pristine $PrC_{60}MA$, followed by 98, 55 and 62 [F $cm^{-3}$] for 95%, 90% and 75% $PrC_{60}MA$, respectively. These values demonstrate a very non-linear trend with a peak value of 103 [F $cm^{-3}$%] in terms of volumetric capacitance per fullerene unit at the 5 : 95 blend, which is an increase of 70% compared to pristine $PrC_{60}MA$. This sharp increase in capacitance, along with the decrease in $PrC_{60}MA$'s mobility (Fig. 3), is most likely a result of the significant decrease in $PrC_{60}MA$ grain size, thereby augmenting the crystallites' surface area and assisting the transport of cations for n-type doping. A similar observation was made in a study about the effect of polydispersity of PSS in PEDOT:PSS blends,[19] where high polydispersity of PSS formed coarse domains with enhanced mobility and reduced capacitance, and low polydispersity caused the formation of fine domains with reduced mobility and high capacitance. It is also in agreement with reports on the effect of nanoporosity on OECT performance in general[8] and specifically on the volumetric capacitance.[43]

While n-type mobility results show similar values in all of the blends and then peaks at 100% PrC60MA (Fig. 3(a)), the n-type capacitance peaks at 5 : 95 and then decreases to ~60 [F $cm^{-3}$] for 100% $PrC_{60}MA$. This result implies that though blending creates fast routes for cation injection and coupling as the fullerene surface area is increased, the polymer phase, when increased above 5% in the blend, either effectively stalls the cation diffusion on their way to dope the fullerene phase or inhibits their coupling with the fullerene crystallites. This creates the observed combined effect of initial overall increased relative number of fullerenes that contribute to the volumetric capacitance, through a peak at 95% $PrC_{60}MA$, followed by a reduction due to stalled ionic diffusion through the pristine material.

### 2.4. Overall microstructure of the system

Integrating the results from previous sections regarding the crystallinity and orientation, transient response time, mobility, capacitance, and spectral signatures, we can now draw a schematic illustration of the structure–property correlation of mixed ionic and electronic conduction in the pristine materials and their studied blends. This simplified schematic is shown in Fig. 6. As suggested before, moving from the pristine fullerene $PrC_{60}MA$, through blends with the polymer p(g2T-TT), all the way to pristine p(g2T-TT) results in: (i) increased homogeneity, with respect to the crystallite distribution throughout the film, (ii) randomization of crystallite orientation, and (iii) the decrease of domain size, overall forming a true bulk-heterojunction structure in the blends. This suggested microstructure is supported by scanning electron microscopy images in Fig. S20 (ESI†). Further evidence can be found in the analysis of the threshold voltages, Fig. S21 (ESI†), which remains unchanged for the fullerene, but becomes more negative for the polymer as its content is reduced, corroborating that doping becomes monotonously harder as polymer chains are scarcer in the film.

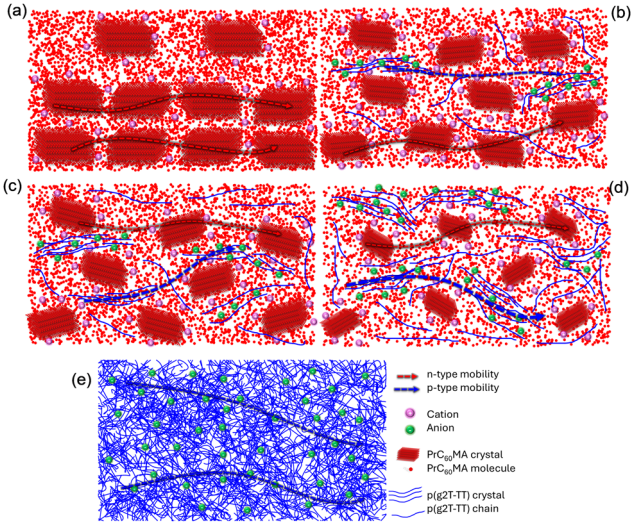


Fig. 6 Microstructure of the p(g2T-TT):$PrC_{60}MA$ system, from (a) $PrC_{60}MA$ through (b)–(d) 5 : 95, 10 : 90, 25 : 75 to (e) p(g2T-TT). Legend attached in the figure.

This microstructure evolution with composition can explain the n-type performance. In the pristine $PrC_{60}MA$ film, there are many oriented large crystallites that reside mostly at the bottom of the film, causing slow OECT and spectral response, high n-type mobility and reasonable capacitance. Upon the addition of 5% wt p(g2T-TT), substantial changes occur: the number and size of the $PrC_{60}MA$ crystallites are reduced, and the paracrystalline disorder of those crystallites increases. The film becomes entirely homogeneous and the changes in $PrC_{60}MA$'s crystalline structure, mainly the increase in overall crystallite surface area, result in the higher n-type capacitance, lower mobility, and faster OECT and spectral response. Moving to the viewpoint of p(g2T-TT) in the 5 : 95 wt% blend – the polymer chains are scarce (5% polymer) and adopt a more planar head-to-tail J-aggregation, resulting in a mobility surprisingly similar to that of the pristine polymer, highest relative capacitance, but a slow response time due to the long way ions have to travel to dope it.

Increasing the polymer amount to 10 wt% does not further reduce $PrC_{60}MA$'s crystallite size, however, their number and preferred orientation decrease. In this blend, the n-type capacitance decreases back to its pristine value and the mobility is unaffected, due to increasing interference of the polymer phase with fullerene doping and a remaining percolation path for electron transport, respectively. The presence of p-type polymer chains in the film becomes more significant and J-aggregation remains similar, therefore p-type mobility increases beyond the pristine values, while OECT ON response time is still very slow.

The richest p-type blend in this study, achieved by increasing the polymer content to 25 wt%, leads to a peak in p-type mobility due to the combined effects of J-aggregation and many

 

percolation paths between polymer chains, as well as a linear increase in p-type capacitance. Regarding the n-type in this blend, $PrC_{60}MA$'s crystallites are now much smaller (about half of their pristine value), less oriented and with a substantial degree of paracrystallinity, though percolation pathways for electrons are still unaffected as the n-type mobility remains the same. OECT response time is the fastest of all blends due to the better p–n balance in the interpenetrating morphology, though still the p-type ON time is slower than pristine values.

The pristine polymer is characterized by a large capacitance due to the high ethylene-glycol content, as well as fair mobility that is a result of lower J-aggregation and higher H-aggregation. In contrast to $PrC_{60}MA$, p(g2T-TT)'s crystallite size is calculated to be only $\sim$8 nm, using the Scherrer equation[44] (experimental eqn (10)) on the first diffraction peak (Fig. S10, ESI†). The OECT response time becomes much faster since now polymer chains are readily available in the film compared to the other dilute-donor blends, yet the spectral response time is slower than that of the 5 : 95 blend. This suggests that in the pristine polymer the doping stage rather than the transport along the channel is the rate determining step.

# 3. Conclusion

In this work we performed a comprehensive investigation of the structure–property relationship in an ambipolar blend based on polymer:fullerene OMIECs. In this system it was found that the blending approach can actually enhance the mobility and capacitance through local chain aggregation and changes in crystallites surface area, respectively. Moreover, the ionic diffusion inside the organic film can be tuned using blending, as it emerges from the comparison between transient response time in spectral measurements and OECTs. The unique microstructural features of this polymer:fullerene system can be expanded to other similar OMIEC systems based on blends. The findings of this research can and should be utilized to further advance the field of ambipolar OMIEC systems based on blends.

# 4. Experimental section

### Materials

Poly(2-(3,3′-bis(2-(2-(2-methoxyethoxy)ethoxy)ethoxy)-[2,2′-bithiophen]-5-yl)thieno [3,2-*b*]thiophene) (p(g2T-TT), $M_n$ = 8.1 kDa, $M_w$ = 18.3 kDa from GPC in DMF at 40 °C) was synthesized by the McCulloch group according to previous reports and used as received.[45] C60,*N*,*N*,*N*-Trimethyl-1-(2,3,4-tris(2-(2-methoxyethoxy)ethoxy)-phenyl)methanaminium monoadduct ($PrC_{60}MA$, Solenne BV), KCl (Sigma-Aldrich Israel Ltd), Diethylzinc (packaged for use in deposition systems, Sigma-Aldrich Israel Ltd) were used as received.

### Film preparation

All substrates were cleaned before film deposition in an ultrasonic bath in acetone, methanol, and isopropanol (15 minutes each) and blow-dried in $N_2$ (99.995%). p(g2T-TT) and $PrC_{60}MA$ were dissolved in chloroform (anhydrous, contains amylene as a stabilizer, $\sim$99%, Sigma-Aldrich Israel Ltd) at concentrations of 5 mg ml$^{-1}$ and either 10 mg ml$^{-1}$ or 30 mg ml$^{-1}$ at room temperature, respectively, and stirred for at least 3 hours before further processing. For blend preparation, pristine material solutions were mixed in the appropriate amounts to achieve 75 : 25, 90 : 10, and 95 : 5 (w : w) blend ratios and stirred for at least 3 hours before further processing. All solutions were spin-coated at room temperature onto substrates at 1000 rpm for 60 s followed by 3000 rpm for 10 s, to obtain 60–70 nm film thicknesses when using 5 mg ml$^{-1}$ p(g2T-TT) and 10 mg ml$^{-1}$ $PrC_{60}MA$. For VPI measurements we prepared thicker films, $\sim$200 nm, using 5 mg ml$^{-1}$ p(g2T-TT) with 500 rpm for 60 s and 30 mg ml$^{-1}$ $PrC_{60}MA$ with 1000 rpm for 60 s. All films were subsequently annealed on a hot plate at 120 °C for 20 minutes. Film preparation was executed entirely under an inert atmosphere inside a glovebox. Film thicknesses were measured using a stylus profilometer (Bruker DektakXT) with a 12.5 μm radius of the needle tip.

### Spectroelectrochemistry (SEC) and cyclic voltammetry (CV)

Fluorine-doped tin oxide (FTO) coated glass (surface resistivity $\sim$7 Ω sq$^{-1}$, Sigma-Aldrich Israel Ltd) was used as a conductive transparent WE and coated with materials as described above. The FTO-coated substrates were dipped in a 0.1 M KCl solution in a glass cuvette (3/G/10, Starna Scientific Ltd) with a Pt wire as CE and an Ag/AgCl pellet (E206 Warner Instruments, LLC) RE. To avoid faradaic side reactions on the FTO surface, the corners of the substrate were masked with Kapton® tape. The setup was put inside a UV-Vis spectrophotometer (Cary 100 Scan, Agilent Technologies, Inc.) and connected to an external potentiostat (Palmsens4, PalmSens BV) as a controller. First, the spectrum was recorded without any external voltage, then 20 cycles of cyclic voltammetry (CV) were performed in the range of +0.3 V → −0.9 V ($V_{WE}$) at a rate of 0.1 V s$^{-1}$ to condition the films. Then each spectrum was recorded after first holding the voltage constant for 30 s. Absorbance change was calculated with respect to $V_{WE}$ = −0.4 V recorded spectrum. To calculate the expected spectrum of the blend a rule of mixtures was applied:

$$\mathrm{Abs}_{calc} = X_{PrC_{60}MA}\cdot\mathrm{Abs}_{PrC_{60}MA} + X_{p(g2T\text{-}TT)}\cdot\mathrm{Abs}_{p(g2T\text{-}TT)} \quad (1)$$

where $X$ is the weight fraction of the respective component.

### Differential absorbance spectra fitting

The differential absorbance data were fitted using the vibronic model developed previously,[32,46] which employs a modified Holstein Hamiltonian treating homopolymer aggregates akin to a molecular crystal with a single phonon mode governing electron–phonon coupling. This model was originally developed for the absorbance data rather than the differential absorbance data, however, in our blend it is impossible to reliably deconvolute the optical contributions of the polymer and small molecule whereas in the differential spectra they are well resolved by the doping voltage. The differential spectra for p(g2T-TT) was taken at $V_{WE}$ = +0.3 V *vs.* $V_{RE}$. According to

eqn (2), this model predicts absorbance as a summation of individual vibronic transitions, with the addition of polaronic features of the same Gaussian shape.

$$A(\omega) = C\sum_{m=0}\frac{e^{-\lambda^2}\lambda^{2m}}{m!}\left(1-\frac{We^{-\lambda^2}}{2E_p}G(\lambda^2;m)\right)^2 \times \Gamma\left(\hbar\omega - E_{00} - mE_p - 0.5W\lambda^{2m}e^{-\lambda^2}\right) - \Gamma_{pol}(\hbar\omega - E_{pol}) \quad (2)$$

where the vibronic factor $G$ is:

$$G(\lambda^2;m) = \sum_{n=0,1\ldots n\neq m}\frac{\lambda^{2n}}{n!(n-m)} \quad (3)$$

And the Gaussian functions are defined as:

$$\Gamma(x) = \frac{1}{\sigma\sqrt{2\pi}}e^{-\frac{x^2}{2\sigma^2}} \quad (4)$$

$$\Gamma_{pol}(x) = C_{pol}e^{-\frac{x^2}{2\sigma_{pol}{}^2}} \quad (5)$$

The free parameters in the fitting procedure were $C$ the vibronic scaling factor, $W$ the exciton bandwidth, $E_p$ the average vibrational energy of multiple phonon modes of symmetric thiophene backbone ring-breathing, $E_{00}$ the 0–0 vibronic transition energy, $\sigma$ the FWHM of vibronic transitions, $C_{pol}$ the polaronic scaling factor, $E_{pol}$ the polaronic energy and $\sigma_{pol}$ the FWHM of the polaronic transition. Following previous studies, $E_p$ was kept in the vicinity of 0.17 eV. The vibronic peaks considered were only 0–0, 0–1, 0–2, 0–3, and 0–4, as the amplitude of the 0–4 transition was already found to be negligible.

Though sometimes kept at 1 for simplicity, $\lambda^2$ was taken as 0.97 in this work since for $\lambda^2 = 1$ the exciton bandwidth $W$ was found to be negative, which is not physical for H-aggregate model when $A_{00}/A_{01} < 1.05$. This methodology was also employed in a recent study.[46] Following the fitting of differential absorbance spectra, the ratio between the peak intensity of the 0–0 and 0–1 transitions was determined.

### Electrochemical impedance spectroscopy (EIS)

Cr/Au square pads (0.0036 $cm^2$) were photolithographically patterned on a microscope glass slide using a method explained elsewhere[47] and spin-coated with the semiconductor solution in chloroform, followed by peeling of a top sacrificial layer of Parylene C. The impedance spectra were recorded with a Potentiostat (PalmSens4, PalmSens BV) in a 3-electrode setup using a 0.1 M KCl solution, Ag/AgCl pellet as RE, and Pt Wire as CE, at a frequency range between 1 MHz and 0.1 Hz. The measurements were performed at DC voltage ranging from 0.3 V to −0.9 V with a step of 0.1 V, and AC amplitude of 10 mV.

After EIS measurement, the capacitance was extracted using two methods. The first method was fitting to an equivalent circuit in the dedicated software (PStrace 5, PalmSens BV) using a simplified Randles Cell R(RC) for p-type and semi-ideal 2-time-constants Voigt Cell R(RC)(RQ) for the n-type. The second method was taking the effective capacitance at 1 Hz using the following equation:

$$C_{eff} = \frac{1}{2\pi f Z''} \quad (6)$$

where $f$ is the frequency and $Z''$ the imaginary part of the measured impedance. In both methods, the capacitance was normalized by the measured film volume to determine volumetric capacitance $C^*$. This latter method was eventually selected to plot and calculate mobility from $\frac{\mu C^*}{C_{eff}}$ as it uses fewer preliminary assumptions since there is no need to fit an equivalent circuit.

### Electrochemical quartz-crystal microbalance (EQCM)

Gold-coated quartz crystal sensors (5 MHz for Q-sense E1/E4, RenLux Crystal Ltd) were used as WE and coated with materials as described above. The sensor was placed in a dedicated cell (QWEM 401, Q-sense Explorer, Biolin Scientific) with a Pt wire CE and Ag/AgCl (3 M KCl) RE. The measurements were performed as follows: first, the QCM response of the bare Au-quartz sensor in air was recorded, then the sensor was coated with the organic layer and again recorded in air; the sensor was put in the module and aqueous 0.1 M KCl solution was continuously pumped into the chamber at a flow rate of 100 µl $min^{-1}$ controlled by a peristaltic pump for 4 hours and the QCM response was recorded again; finally CV in the range +0.3 V to −0.9 V was performed for several cycles at a scan rate of 10 mV $s^{-1}$ and the frequencies recorded over 7 overtones. As the films are thin they were treated as rigid, therefore we could use the Sauerbrey equation (eqn (7)) to convert $\frac{\Delta f}{n}$ to the change in areal mass $\Delta m$:

$$\Delta m = -C\frac{\Delta f}{n} = -5.9\cdot\Delta f\left[\frac{ng}{cm^2}\right] \quad (7)$$

This equation uses $C = 17.7\left[\frac{ng}{cm^2\ Hz}\right]$ as a constant for a 5 MHz crystal, a constant that is dependent on the wave velocity in quartz plate, the density of quartz and the fundamental resonance frequency. Only the 3rd overtone was used in calculations; therefore, it is put into eqn (2) as well as $n = 3$.

### Vapor phase infiltration (VPI)

Vapor phase infiltration (VPI) process of zinc oxide into the organic films was performed in an atomic layer deposition system (Savannah® S200, Veeco Instruments Inc.). Silicon substrates were cleaned followed by film deposition *via* spin-coating as described above. The samples were then put in the ALD system and exposed to diethylzinc vapors and DI water in a pulse-exposure-purge sequence. One cycle of the process consisted of pulsing the precursors into the reaction chamber for 0.02 s (diethylzinc) and 0.04 s (DI water), with 20 s exposure time for each. Each exposure was followed by a 25 s purge step, each precursor step was applied twice before the sequence of the second began. The cycle was repeated 80 times, with $N_2$

 

(99.99%) as the carrier and purging gas. The reaction chamber was heated to 60 °C and the base flow rate of the reactor was 20 sccm.

### High resolution scanning electron Mmcroscopy (HRSEM)

High-resolution scanning electron microscopy (HRSEM) cross-section images of films on Silicon substrates were recorded using a Zeiss Ultra-Plus FEG-SEM at 1.5 keV and WD ~ 2.5 mm, with a Back-scattered Electrons (BSE) detector for *Z*-contrast observation between ZnO grains and unstained organic regions in the film.

### X-ray diffraction (XRD)

Out-of-plane $\theta/2\theta$ XRD measurements of films on silicon substrates were recorded using a Rigaku SmartLab 9 kW X-ray diffractometer with Scintillation Counter (SC-70) 0D detector and Cu Kα radiation ($\lambda$ = 1.5418 Å). Scan range was $1^\circ < 2\theta < 30^\circ$ with a 0.01° step and speed of 3° $min^{-1}$. For $PrC_{60}MA$ 7 orders of lamellar stacking peaks (00*l*) were observed at $2\theta \approx n{\cdot}3.1^\circ$, where $n$ is the order number. The conversion of $2\theta$ to *d*-space was performed using regular Bragg's equation:

$$n\lambda = 2d{\cdot}\sin\theta \tag{8}$$

To calculate the coherence length, we applied a pseudo-Voigt function fitting on each peak of $PrC_{60}MA$ (in both the pristine and blend films). The fitting function is of the form of a linear combination of a Gaussian and a Lorentzian with a similar FWHM:

$$I = I_0 + A\left[m_u\frac{2}{\pi}\frac{w}{4(q-q_c)^2+w^2} + (1-m_u)\frac{\sqrt{4\ln 2}}{w\sqrt{\pi}}e^{-\frac{4\ln 2}{w^2}(q-q_c)^2}\right] \tag{9}$$

where $I$ is the overall intensity, $I_0$ offset intensity, $A$ the area, $\mu$ profile shape factor, $q$ the scattering vector, $q_c$ scattering vector peak center, and w the FWHM of the peak. Since finite grain size and cumulative disorder is common in organic films, diffraction peaks that belong to the same set of crystal planes, namely (00*l*), displayed a successive broadening at higher orders. The extracted FHWM was plotted against the square peak order $m^2$ and the extrapolated intersection at $m^2 = 0$ was taken as $\frac{2\pi}{L_c}$, where $L_c$ is the coherence length, following a method of analysis described elsewhere.[48]

While less accurate, the simplified Scherrer equation offers the calculation of coherence length using only the first peak and the following relation:

$$L_c = \frac{2\pi K}{\Delta_q} \tag{10}$$

where $K$ is the shape factor (typically 0.8–1) usually used as 0.94, and $\Delta_q$ is the FWHM of the diffraction peak.[44] This equation was used for the first diffraction peak of p(g2T-TT) as it only had 2 visible peak in the X-ray diffraction measurement.

For 2D-GIWAXS measurements we used Rigaku SmartLab 9 kW X-ray diffractometer with Cu Kα radiation ($\lambda$ = 1.54186 Å), equipped with a HyPix-3000 2D detector and an aperture slit installed. Scan range of the detector was up to $2\theta = 30^\circ$ horizontal and up to $2\theta = 35^\circ$ vertical, incident angle $\omega = 0.2^\circ$ and scan time of 30 minutes.

### Organic electrochemical transistors (OECTs) device fabrication and measurement

Ultra-flat quartz-coated glass 15 mm × 20 mm substrates were cleaned as described above and blow-dried in $N_2$ (99.995%). Then, substrates were placed in an OFET shadow mask (E291, Ossila Ltd) where each substrate consists of 5 identical transistors with $W$ = 1000 μm, $L$ = 30 μm. The assembly was put inside a metal thermal evaporator (Edwards Auto 500), where 5 nm chromium and 50 nm gold were evaporated at a rate of 0.03–0.06 nm $s^{-1}$ at a pressure of $\sim 6 \times 10^{-6}$ Torr. After the evaporation of metal contacts, the substrates were additionally cleaned for 15 minutes in isopropanol in an ultrasonic bath, blow-dried with $N_2$ gun, and coated with the organic film. The film was dry-wiped from most of the metal contacts except for the channel area to minimize device crosstalk. Finally, Kapton® tape was used to manually mask the areas where the metal contacts were exposed to avoid contact between electrolyte and metal.

A manual probe station was used for all electrical measurements. For OECT device characterization, a dual-channel source measure unit (SMU) (B2902A, Keysight Technologies, Inc.) was used with a dedicated software (EasyExpert group+). The SMU was connected to source & drain gold contacts as well as Ag/AgCl pellet (E206 Warner Instruments, LLC) that was used as the gate electrode. The electrolyte was 0.1 M KCl and dropped onto the devices before measurement. Output and Transfer curves were acquired with a double-sweep measurement. For output curves the sweeping conditions were as follows: the drain voltage $V_d$ was swept in steps of 13 mV at a rate of 0.1 V $s^{-1}$, in the range of $-0.05\ V < V_d < +0.6\ V$ for n-type and $-0.6\ V < V_d < +0.05\ V$ for p-type; the gate voltage $V_g$ curves were recorded in the range $+0.4\ V < V_g < +0.9\ V$ for n-type and $-0.3\ V < V_g < +0.2\ V$ for p-type, with a 0.05 V step size. For transfer curves the sweeping conditions were as follows: the drain voltage was set to either +0.4 V for n-type or –0.4 V for p-type; the gate voltage was swept in steps of 1 mV at a rate of ~0.01 V $s^{-1}$, in a range of $+0.4\ V < V_g < +0.9\ V$ for n-type and $-0.3\ V < V_g < +0.2\ V$ for p-type. For each ambipolar device the sweeping program was Output n-type → Transfer n-type → Output p-type → Transfer p-type, cycled 3 times according to the conditions described above. Calculations were based on an average of 4 devices per composition, each device averaged over 3 operation cycles, using a custom-made MATLAB script. Transconductance at maximum $V_g$ for each polarity (–0.3 V for p-type, +0.9 V for n-type), and the device figure-of-merit $\mu C^*$ were calculated from the transfer curves according to eqn (11):

$$g_m = \frac{\partial I_d}{\partial V_g} = \frac{Wd}{L}\mu C^*\left|V_{th} - V_g\right| \tag{11}$$

The threshold voltage $V_{th}$ was calculated by using a linear fit of $\sqrt{I_d}$ *vs.* $V_g$ from the transfer curves and extraction of the intercept point between the fit and $\sqrt{I_d} = 0$.

### OECT stability measurement and electrical transient response time

For stability measurements, the same setup as OECT characterization was used, yet square wave pulses were applied instead of regular sweep. The pulses were applied in another dedicated software (Quick I/V Measurement). The gate voltages for OFF current and ON current were determined with respect to the threshold voltage, to maintain the same driving force for doping and de-doping in different compositions. The gate voltage was determined as such: $V_{g,OFF} = V_{th} - 0.1$ V; $V_{g,ON} = V_{th} + 0.25$ V.

The drain voltage was $V_d = +0.4$ V for n-type and $V_d = -0.4$ V for p-type. The gate voltage order was p-type OFF → p-type ON → p-type OFF → n-type OFF → n-type ON → n-type OFF. Response time for the ON step of all compositions was extracted using an average weighting of biexponential time constants:

$$I_d = I_{d,0} + A_1 \exp\left(-\frac{t - t_0}{\tau_1}\right) + A_2 \exp\left(-\frac{t - t_0}{\tau_2}\right) \quad (12)$$

$$\tau_{ON} = \left(\frac{A_1}{A_1 + A_2}\right)\tau_1 + \left(\frac{A_2}{A_1 + A_2}\right)\tau_2 \quad (13)$$

Response time for the OFF step of all compositions was extracted using monoexponential fitting:

$$I_d = I_{d,0} + B \exp\left(-\frac{t}{\tau_{OFF}}\right) \quad (14)$$

The degradation% of each device is calculated as follows:

$$\%\text{Degradation} = \frac{\max(I_{360}) - \max(I_{40})}{\max(I_{40})} \times 100 \quad (15)$$

where $\max(I_{40})$ is the peak current in the 40th cycle and $\max(I_{360})$ is the peak current in the 360th cycle.

### Vis-NIR spectroelectrochemistry

The measurements were conducted using a custom-built setup that simultaneously measures current and spectra with a resolution of 8 ms, consisting of a halogen light source (HL-2000, Ocean Insight), Flame UV-Vis and Flame NIR spectrometers (Ocean Insight) triggered by a digital delay/pulse generator (DG535, Stanford Research Systems). Films of the n-type, p-type, and their blends (approx. 20, 60, and 200 nm thick) were immersed in 0.1 M KCl aqueous electrolyte with an Ag/AgCl pellet electrode. The bias between the Ag/AgCl quasi-reference electrode and the film was applied and recorded using a data acquisition card (USB-6008, National Instruments), while the transient response current was converted into voltage using a low noise current preamplifier (SR570, Stanford Research Systems) and measured with the same data acquisition card. To ensure reproducibility, the films underwent five CV cycles before the experiments. Time-resolved measurements of the doping/dedoping steps were performed by applying 1 s square voltage pulses ranging from −0.9 V to +0.3 V in 0.1 V increments, with a dedoping voltage of −0.4 V applied between each step (Fig. S1, ESI†).

### MCR decomposition

MCR decomposition was conducted on the raw spectra using pyMCR, a Python-based library. In summary, the spectral data is described by a matrix $D$, and the MCR algorithm uses iterative alternating regression to solve the following equation:

$$D = CS^T + \varepsilon \quad (16)$$

where $C$ is the concentration matrix, $S$ is the spectral signatures matrix and $\varepsilon$ is the error matrix, which is optimized to be minimal and account for noises, shifts, and other features not considered in the decomposition. The MCR analysis does not provide absolute concentration values or species absorbance cross-section, and therefore the results shown here are not quantitative.

We decomposed the spectra of the blends (films of approx. 20, 60, and 180 nm thickness) into two species signatures and their concentrations. The spectra of the pristine n- and p-type films (with approx. 20, 60 nm, and 130 nm (for p-) or 200 nm (for n-type)) were decomposed into one species and its concentration.

### Crystalline structure simulation

The approximation of the tetragonal crystalline structure of $PrC_{60}MA$ was performed using Avogadro: an open-source molecular builder and visualization tool, Version 1.2.0, **https://avogadro.cc/**. The input parameters were $a = b = 10$ Å, $c = 25$ Å, force field UFF and the energy reduction algorithm was set to steepest descent.

## Data availability

The data supporting this article has been included as part of the ESI.†

## Conflicts of interest

There are no conflicts to declare.

## Acknowledgements

This project was partially funded by the European Union's Horizon 2020 research and innovation program under grant agreement no 964677 (MITICS). The authors thank Professor Jonathan Rivnay and Dr Reem Rashid for contributing the substrates used for EIS measurements, and Garret LeCroy for his help with fitting spectroelectrochemical measurements. IMCC acknowledges financial support from KAUST Office of Sponsored Research CRG10, by EU Horizon2020 grant agreement no 952911, BOOSTER, as well as EPSRC Projects EP/T026219/1, EP/W017091/1 and EP/X038777/1.

 

## References

1 S. Fabiano, L. Flagg, T. C. Hidalgo Castillo, S. Inal, L. G. Kaake, L. V. Kayser, S. T. Keene, S. Ludwigs, C. Muller, B. M. Savoie, B. Lüssem, J. L. Lutkenhaus, M. Matta, D. Meli, S. N. Patel, B. D. Paulsen, J. Rivnay and J. Surgailis, *J. Mater. Chem. C*, 2023, **11**, 14527–14539.
2 G. Malliaras and I. McCulloch, *Chem. Rev.*, 2022, **122**, 4323–4324.
3 H. Kim, Y. Won, H. W. Song, Y. Kwon, M. Jun and J. H. Oh, *Adv. Sci.*, 2024, **11**, 2306191.
4 I. B. Dimov, M. Moser, G. G. Malliaras and I. McCulloch, *Chem. Rev.*, 2022, **122**, 4356–4396.
5 S. T. Keene, V. Gueskine, M. Berggren, G. G. Malliaras, K. Tybrandt and I. Zozoulenko, *Phys. Chem. Chem. Phys.*, 2022, **24**, 19144–19163.
6 J. Surgailis, A. Savva, V. Druet, B. D. Paulsen, R. Wu, A. Hamidi-Sakr, D. Ohayon, G. Nikiforidis, X. Chen, I. McCulloch, J. Rivnay, S. Inal, A. Hamidi-Sakr, D. Ohayon, G. Nikiforidis, X. Chen, I. McCulloch, J. Rivnay and S. Inal, *Adv. Funct. Mater.*, 2021, **31**, 2010165.
7 Z. S. Parr, J. Borges-González, R. B. Rashid, K. J. Thorley, D. Meli, B. D. Paulsen, J. Strzalka, J. Rivnay and C. B. Nielsen, *Adv. Mater.*, 2022, **34**, 2107829.
8 X. Wu, T. L. D. Tam, S. Chen, T. Salim, X. Zhao, Z. Zhou, M. Lin, J. Xu, Y. L. Loo and W. L. Leong, *Adv. Mater.*, 2022, **34**, 2206118.
9 E. Stein, O. Nahor, M. Stolov, V. Freger, I. M. Petruta, I. McCulloch and G. L. Frey, *Nat. Commun.*, 2022, **13**, 5548.
10 P. R. Warren, J. F. M. Hardigree, A. E. Lauritzen, J. Nelson and M. Riede, *AIP Adv.*, 2019, **9**, 35202.
11 Y. Hayashi, H. Kanamori, I. Yamada, A. Takasu, S. Takagi and K. Kaneko, *Appl. Phys. Lett.*, 2005, **86**, 1–3.
12 H. Frankenstein, E. Stein, M. Stolov, M. K. Khristosov, V. Freger and G. L. Frey, *J. Mater. Chem. C*, 2021, **9**, 7765–7777.
13 S. Yamamoto and G. G. Malliaras, *ACS Appl. Electron. Mater.*, 2020, **2**(7), 2224–2228.
14 M. Barker, T. Nicolini, Y. Al Yaman, D. Thuau, O. Siscan, S. Ramachandran, E. Cloutet, C. Brochon, L. Richter, O. J. Dautel, G. Hadziioannou and N. Stingelin, *Mater. Horiz.*, 2023, **10**, 248–256.
15 A. F. Paterson, A. Savva, S. Wustoni, L. Tsetseris, B. D. Paulsen, H. Faber, A. Hamid Emwas, X. Chen, G. Nikiforidis, T. C. Hidalgo, M. Moser, I. Petruta Maria, J. Rivnay, I. McCulloch, T. D. Anthopoulos and S. Inal, *Nat. Commun.*, 2020, **11**, 3004.
16 V. N. Le, J. H. Bombile, G. S. Rupasinghe, K. N. Baustert, R. Li, I. P. Maria, M. Shahi, P. Alarcon Espejo, I. McCulloch, K. R. Graham, C. Risko and A. F. Paterson, *Adv. Sci.*, 2023, **10**(27), 2207694.
17 Z. S. Parr, R. B. Rashid, B. D. Paulsen, B. Poggi, E. Tan, M. Freeley, M. Palma, I. Abrahams, J. Rivnay and C. B. Nielsen, *Adv. Electron. Mater.*, 2020, **6**, 2000215.
18 G. LeCroy, C. Cendra, T. J. Quill, M. Moser, R. Hallani, J. F. Ponder, K. Stone, S. D. Kang, A. Y.-L. L. Liang, Q. Thiburce, I. McCulloch, F. C. Spano, A. Giovannitti and A. Salleo, *Mater. Horiz.*, 2023, **10**, 2568–2578.
19 C. Y. Lo, Y. Wu, E. Awuyah, D. Meli, D. M. Nguyen, R. Wu, B. Xu, J. Strzalka, J. Rivnay, D. C. Martin and L. V. Kayser, *Polym. Chem.*, 2022, **13**, 2764–2775.
20 M. Baghgar, J. A. Labastide, F. Bokel, R. C. Hayward and M. D. Barnes, *J. Phys. Chem. C*, 2014, **118**, 2229–2235.
21 J. Liu, B. van der Zee, R. Alessandri, S. Sami, J. Dong, M. I. Nugraha, A. J. Barker, S. Rousseva, L. Qiu, X. Qiu, N. Klasen, R. C. Chiechi, D. Baran, M. Caironi, T. D. Anthopoulos, G. Portale, R. W. A. Havenith, S. J. Marrink, J. C. Hummelen and L. J. A. Koster, *Nat. Commun.*, 2020, **11**, 5694.
22 M. Causa', I. Ramirez, J. F. Martinez Hardigree, M. Riede and N. Banerji, *J. Phys. Chem. Lett.*, 2018, **9**, 1885–1892.
23 M. M. Khaled, R. T. Carlin, P. C. Trulove, G. R. Eaton and S. S. Eaton, *J. Am. Chem. Soc.*, 1994, **116**, 3465–3474.
24 J. Guo, S. E. Chen, R. Giridharagopal, C. G. Bischak, J. W. Onorato, K. Yan, Z. Shen, C.-Z. Li, C. K. Luscombe and D. S. Ginger, *Nat. Mater.*, 2024, **23**, 656–663.
25 E. Stein, O. Nahor, M. Stolov, V. Freger, I. M. Petruta, I. McCulloch and G. L. Frey, *Nat. Commun.*, 2022, **13**, 5548.
26 S. T. Keene, J. E. M. Laulainen, R. Pandya, M. Moser, C. Schnedermann, P. A. Midgley, I. Mcculloch, A. Rao and G. G. Malliaras, *Nat. Mater.*, 2023, **22**, 1121–1127.
27 B. Balambiga, R. Dheepika, P. Devibala, P. M. Imran and S. Nagarajan, *Sci. Rep.*, 2020, **10**, 1–13.
28 S. S. Cheng, P. Y. Huang, M. Ramesh, H. C. Chang, L. M. Chen, C. M. Yeh, C. L. Fung, M. C. Wu, C. C. Liu, C. Kim, H. C. Lin, M. C. Chen and C. W. Chu, *Adv. Funct. Mater.*, 2014, **24**, 2057–2063.
29 J. Y. Kim and C. D. Frisbie, *J. Phys. Chem. C*, 2008, **112**, 17726–17736.
30 Y. Zhang, G. Ye, T. P. A. A. van der Pol, J. Dong, E. R. W. W. van Doremaele, I. Krauhausen, Y. Liu, P. Gkoupidenis, G. Portale, J. Song, R. C. Chiechi and Y. van de Burgt, *Adv. Funct. Mater.*, 2022, **32**, 2201593.
31 D. Ohayon, A. Savva, W. Du, B. D. Paulsen, I. Uguz, R. S. Ashraf, J. Rivnay, I. McCulloch and S. Inal, *ACS Appl. Mater. Interfaces*, 2021, **13**, 4253–4266.
32 F. C. Spano, *J. Chem. Phys.*, 2005, **122**(23), 234701.
33 J. Liu, B. van der Zee, R. Alessandri, S. Sami, J. Dong, M. I. Nugraha, A. J. Barker, S. Rousseva, L. Qiu, X. Qiu, N. Klasen, R. C. Chiechi, D. Baran, M. Caironi, T. D. Anthopoulos, G. Portale, R. W. A. Havenith, S. J. Marrink, J. C. Hummelen and L. J. A. Koster, *Nat. Commun.*, 2020, **11**, 5694.
34 J. Dong, S. Sami, D. M. Balazs, R. Alessandri, F. Jahani, L. Qiu, S. J. Marrink, R. W. A. Havenith, J. C. Hummelen, M. A. Loi and G. Portale, *J. Mater. Chem. C*, 2021, **9**, 16217–16225.
35 S. Marina, E. Gutierrez-Fernandez, J. Gutierrez, M. Gobbi, N. Ramos, E. Solano, J. Rech, W. You, L. Hueso, A. Tercjak, H. Ade and J. Martin, *Mater. Horiz.*, 2022, **9**, 1196–1206.
36 T. Sarkar, S. A. Schneider, G. Ankonina, A. D. Hendsbee, Y. Li, M. F. Toney and G. L. Frey, *Chem. Mater.*, 2020, **32**, 7338–7346.
37 J. F. Chang, J. Clark, N. Zhao, H. Sirringhaus, D. W. Breiby, J. W. Andreasen, M. M. Nielsen, M. Giles, M. Heeney and I. McCulloch, *Phys. Rev. B: Condens. Matter Mater. Phys.*, 2006, **74**, 115318.

38 T. J. Quill, G. LeCroy, D. M. Halat, R. Sheelamanthula, A. Marks, L. S. Grundy, I. McCulloch, J. A. Reimer, N. P. Balsara, A. Giovannitti, A. Salleo and C. J. Takacs, *Nat. Mater.*, 2023, **22**, 362–368.
39 G. M. Paternò, M. W. A. Skoda, R. Dalgliesh, F. Cacialli and V. García Sakai, *Sci. Rep.*, 2016, **6**, 1–7.
40 L. M. Andersson, *Org. Electron.*, 2011, **12**, 300–305.
41 D. Gao, B. Djukic, W. Shi, C. R. Bridges, L. M. Kozycz and D. S. Seferos, *ACS Appl. Mater. Interfaces*, 2013, **5**, 8038–8043.
42 S. Amand, M. Musiani, M. E. Orazem, N. Pébère, B. Tribollet and V. Vivier, *Electrochim. Acta*, 2013, **87**, 693–700.
43 S.-M. M. Kim, C.-H. H. Kim, Y. Kim, N. Kim, W.-J. J. Lee, E.-H. H. Lee, D. Kim, S. Park, K. Lee, J. Rivnay and M.-H. H. Yoon, *Nat. Commun.*, 2018, **9**, 1–9.
44 B. E. Warren, *X-Ray Diffraction*, Dover Publications, Inc., New York, 1990.
45 A. Giovannitti, D.-T. Sbircea, S. Inal, C. B. Nielsen, E. Bandiello, D. A. Hanifi, M. Sessolo, G. G. Malliaras, I. McCulloch and J. Rivnay, *Proc. Natl. Acad. Sci. U. S. A.*, 2016, **113**, 12017–12022.
46 G. LeCroy, C. Cendra, T. J. Quill, M. Moser, R. Hallani, J. F. Ponder, K. Stone, S. D. Kang, A. Y. Liang, Q. Thiburce, I. McCulloch, F. C. Spano, A. Giovannitti and A. Salleo, *Mater. Horiz.*, 2023, **10**, 2568–2578.
47 M. Sessolo, D. Khodagholy, J. Rivnay, F. Maddalena, M. Gleyzes, E. Steidl, B. Buisson and G. G. Malliaras, *Adv. Mater.*, 2013, **25**, 2135–2139.
48 J. Rivnay, S. C. B. Mannsfeld, C. E. Miller, A. Salleo and M. F. Toney, *Chem. Rev.*, 2012, **112**, 5488–5519.

 